Regulating the Growth of Cesium Lead Bromide Quantum Dots at a Liquid/Liquid Interface Constrained in a Micropipette

Sohom Chandra[a], Chenjia Mi [a], Zongkai Peng[a], Jack Wilton[a], Hamidreza Shabgard[b], Zhibo Yang[a], Yitong Dong*[a], [c]

[a] S. Chandra, C. Mi, Z. Peng, J. Wilton, Prof. Z. Yang, Prof. Y. Dong
Department of Chemistry and Biochemistry.
The University of Oklahoma
Norman, OK 73019, USA

[b] Prof. H. Shabgard
Aerospace and Mechanical Engineering,
The University of Oklahoma
Norman, OK 73019, USA

[c] Prof. Y. Dong
Centre for Quantum Research and Technology,
The University of Oklahoma
Norman, OK 73019, USA
Email: Yitong.Dong-1@ou.edu

Supporting information for this article is given via a link at the end of the document.

Abstract: Colloidal all-inorganic lead halide perovskite quantum dots (QDs) are high-performance light-emitting materials with size-dependent optical properties and can be readily synthesized by mixing ionic precursors. However, the low formation energy of the perovskite lattice makes their growth too fast to control under regular reaction conditions. We report diffusion-regulated $CsPbBr_3$ perovskite QD growth on a nanometer-sized liquid/liquid (L/L) interface supported in a micropipette tip without long-chain organic ligands. The precursors were divided into two immiscible solutions across the L/L interface to avoid additional nucleation, and the QD growth kinetics are regulated by the constrained cationic diffusion field depending on the size of the micropipette tip. QDs with unprecedentedly small sizes (2.7 nm) were obtained due to the slowed-down growth rates. Our synthesis approach demonstrates the potential of micro-controlled colloidal QD synthesis for mechanistic studies and micro-fabrications.

Lead halide perovskite nanocrystals (NCs) have experienced extensive studies in the past decade due to their high luminescence efficiency, large absorption cross sections, and narrow photoluminescence (PL) linewidths.[1-3] These exotic optical properties have facilitated the rapid development of highly efficient light-emitting diodes with enhanced color purity.[4-6] In addition, collective exciton behavior, such as super-fluorescence, has also been demonstrated in perovskite QD assemblies.[7-9] One distinct feature of perovskite QDs is that they grow much more rapidly at even room temperatures compared to conventional II-VI QDs. This stems from the low formation energy of highly ionic perovskite lattices.[10] The sub-seconds growth rate of perovskite QDs has posed challenges in size control and arresting intermediate products to scrutinize the QD growth mechanisms. A series of approaches have been attempted to suppress the growth of perovskite NCs. For example, by diluting the precursor solution or using a microfluidic platform, perovskite NC growth has been delayed for analyzing the reaction mechanism.[11,12] However, the reaction rate is still fast (nucleation and growth complete within ~ 5 seconds)[11,13]. Varying reaction environments to reduce precursor reactivities can also dramatically slow down the QD growth[14-17] but can alter the growth mechanism and generate 2D and 1D nanostructures.[18] Nevertheless, it is still difficult to regulate lead halide perovskite QD growth, especially at the early stage when the QD sizes are small.[19]

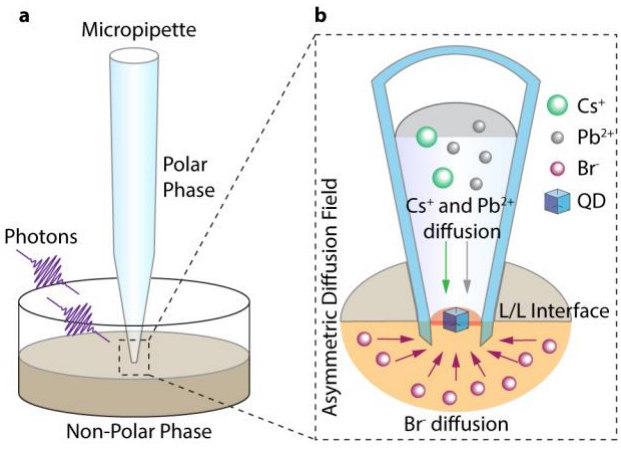

Scheme 1. Schematic illustration of the synthesis of $CsPbBr_3$ QDs on a nano-confined interface. a) The micropipette is filled with an *N,N*-dimethylformamide (DMF) solution containing the lead acetate and cesium acetate precursors, and its tip is immersed in bromobenzene. The bromide precursors are produced by photolysis of bromobenzene once a 405 nm laser illuminates the tip area. b) The asymmetric diffusion field created by the micropipette. Diffusions of cationic precursors inside the micropipette are constrained, whereas the diffusion of the bromide precursors is hemispherical and less restricted.

The kinetically regulated growth of colloidal QDs is often described by the LaMer model.[20-22] In this model, supersaturated precursors nucleate first, followed by a diffusion-controlled QD growth that consumes the remaining precursors. Ostwald ripening happens upon further consumption of precursors, where larger

QDs grow and smaller QDs disintegrate. The key to obtaining homogeneous and controlled QD growth is the separation of nucleation and diffusion-controlled growth.[22] However, the perovskite QD growth is usually accompanied by continuous nucleation events. To overcome this challenge, inhomogeneous reactions that can delay precursor mixing to avoid excessive nucleation have been applied to organic-inorganic halide perovskite NCs.[23] Recently, controllable growth of size-tunable $CsPbBr_3$ QDs was achieved by sustainably releasing Pb precursors.[24] The (Trioctylphosphine oxide) TOPO-Pb complex undergoes equilibrium with the metastable monomer, $Cs[PbBr_3]$, which slowly converts to QDs. This self-limited monomer availability enabled nucleation and growth isolation. Later studies also revealed that metastable perovskite nanoclusters also regulate the growth of perovskite QDs[25,26]

In addition to reactivity control, other chemicals, such as strongly coordinating ligands like TOPO and Octylphosphonic acid, have been used to terminate the reaction and stabilize the NCs.[27,28] Oleylamine/oleic acid acid-base pair was first employed to perovskite QD synthesis and exhibited promise for synthetic control.[29,30] Over the past decade, ligand binding group and ligand tail engineering have been explored to enhance PL efficiency and photostability of perovskite QDs.[31-33] It should also be noted that ligands also play an important role in controlling the anisotropy of the perovskite NCs.[34] However, interaction between ligands and perovskites is highly dynamic: the long-chain organic ligands often form active chemical equilibria with QD surface ions, further complicating the growth kinetics.[35] To date, suppressing the reactivity of precursors is still necessary to slow perovskite QD growth for kinetic studies and obtain very small (< 6 nm) QDs.

Confining crystallizations in a micropipette has been reported recently[36-38]. Typically, nucleation is triggered by an electrochemical stimulus at a micropipette tip dipped in a homogeneous solution containing precursor ions. Single crystals (from sub-μm to ~ tens of μm) will be generated. The narrow pipette tip with a size comparable to the crystal facilitates the study of crystal nucleation by monitoring the change in the ion current blocked by the crystal. However, nanocrystal growth that requires the separation of nucleation can hardly be achieved in a homogeneous solution, especially for perovskite QDs that nucleate nearly barrierless and grow large in seconds.

Here, we report a micro-synthesis method for $CsPbBr_3$ QDs that physically isolates the nucleation from growth processes by creating a static interface that separates different precursors into two immiscible solvents. The nano-sized L/L interface limits the QD nucleation and prevents unwanted precursor mixing. The constrained diffusion field in the micropipette[39] can sustainably deliver precursors and significantly retard the QD growth. Without the need for low precursor concentrations and long-chain organic ligands, the growth time of $CsPbBr_3$ QD was successfully extended to 10-15 mins using the L/L interface. The reaction rate can be easily regulated by changing the size of the pipettes. QDs can be conveniently arrested by retracting the micropipette from the non-polar phase. In-situ photoluminescence (PL) spectroscopic study unraveled successful growth regulation following the LaMer model. Our work directly probes the reaction kinetics of perovskite QD growth without the dynamic surface ligand binding interferences. Our method can produce size-controlled perovskite QDs at dedicated locations for microfabrication, providing a platform for individually tweaking reaction precursors for mechanistic studies.

The micropipette and QD growth regulated by asymmetric diffusion fields are illustrated in Scheme 1. The micropipette is filled with the polar phase: an *N, N*-dimethylformamide (DMF) solution containing cesium acetate and lead acetate. The pipette tip is immersed in bromobenzene, which acts as both the non-polar phase and the bromide source. An objective lens focuses a 405 nm *cw* (continuous wave) laser on the tip area to excite the QDs generated on the L/L interface and collect their photoluminescence (PL) emissions. The focused laser beam also induces the photolysis of bromobenzene to provide bromide ions for QD growth.[40,41] QD generation, therefore, is likely to be restricted at the L/L interface where cationic and anionic precursors meet each other. The open end of the pipette was sealed to maintain the pressure inside and suppress potential L/L interface migrations. (Details in Supporting Information, Methods, and Figure S2.) The laser-induced precursor generation provides a convenient means to switch the reaction on and off. The PL spectra of QDs grown on the interface are recorded in situ using a fluorescence microscope equipped with a modular spectrometer (Supporting Information, Figure S1). It is also worth mentioning that long-chain organic ligands are not introduced into the system. Therefore, the QDs are unlikely to degrade from ligand-precursor ions equilibria[35,42]. The exposure of the ionic QD surface also prevented them from entering the organic phase.

The micropipette supporting the L/L interface was fabricated by pulling apart a glass microcapillary (without a filament) using a laser puller. Figures 1a, 1b, and 1c show the SEM images of three micropipettes with decreasing tip sizes. The pipettes exhibit a conical tip shape, which is necessary to constrain the diffusion field inside the micropipette. The orifice diameter is determined by the magnified images of the same pipettes (Figures 1d, 1e, and 1f). In this study, micropipettes with three different opening sizes,1600 nm (M1), 1200 nm (M2), and 800 nm (M3), are fabricated by changing the parameters on the laser puller (Details in Supporting Information, Methods). The tip size deviation is estimated to be ≤6% after imaging ten individual M3 pipettes (Figure S3). The orifice size of the micropipette also determines the lateral size of the L/L interface. The narrow tip shank and the tip aperture constrains the diffusion field of cations, leading to slower precursor diffusions, which will be discussed later.

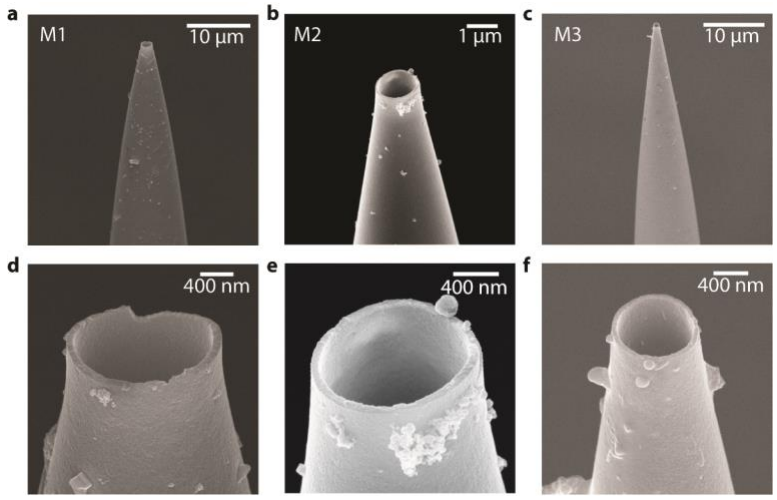

Figure 1. Scanning Electron Microscopy (SEM) images of micropipettes with three different tip sizes. a) - c) Conical shape of the micropipettes. d) - f) close-view of micropipette openings. M1, M2, and M3's tip sizes are ~ 1600 nm, 1200 nm, and 800 nm, respectively.

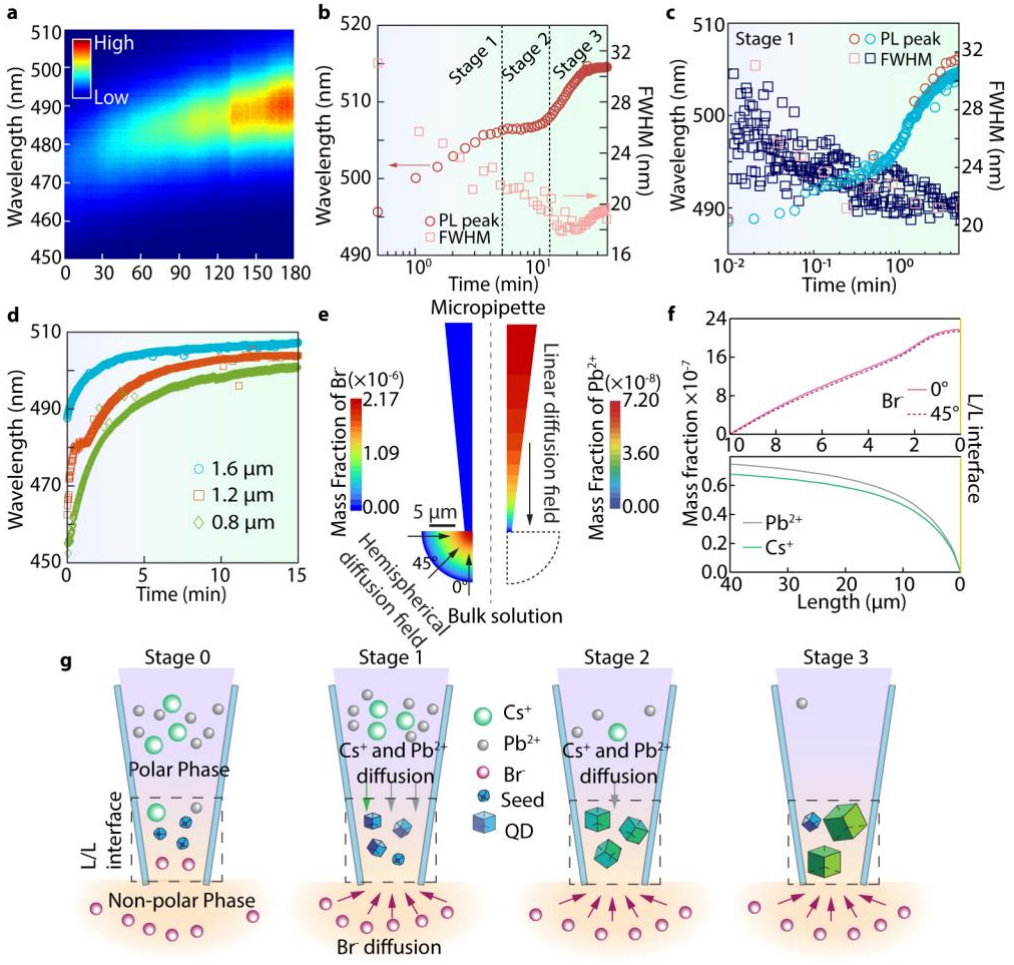

Figure 2. Growth kinetics of $CsPbBr_3$ QDs at the L/L interface. a) In-situ reaction time-dependent PL spectra measured using the M3 pipette. The QDs exhibit a red-shifting PL peak over time, accompanied by increasing PL intensity. b) PL peak and FWHM time trace for M1 showing different stages of growth. Three discrete stages are observed, which are represented as stage 1, stage 2, and stage 3. c) PL peak and FWHM time traces for two separate M1 with different temporal resolutions demonstrating the diffusion-controlled growth (Stage 1) of the QDs. The measurements with spectra recorded at intervals of 600 ms (higher temporal resolution) and intervals of 30 s (lower temporal resolution) exhibit a similar trend for the PL peak shift as well as the FWHM over time. d) PL peak time trace for M1, M2, and M3 showing the change in growth kinetics due to the change in tip size. e) Finite volume simulation illustrating the different diffusion fields that exist inside and outside the micropipette. Ions inside the pipette follow a linear diffusion field, whereas the ions in the bulk solution follow a hemispherical diffusion field. f) Mass fractions of Br^-, Cs^+ and Pb^{2+} obtained from finite volume simulations. The L/L interface is indicated by the yellow line (marked as '0' µm). The Br^- mass fraction at 0° with the pipette tip and at 45° with the pipette tip are relatively equal, indicating a homogeneous Br^- flux towards the L/L interface from all directions in the non-polar reservoir. The Cs^+ and Pb^{2+} exhibit a linear diffusion field that extends over a longer length inside the pipette (40 µm). g) Schematic illustration showing

the proposed QD growing status at stage 0 (QD seed generation at the L/L interface area), stage 1 (diffusion-controlled QD growth on existing seeds), stage 2 (precursor depletion), and stage 3 (Ostwald ripening).

In-situ PL spectra collected from QDs grown inside the tip area are shown in Figure 2a. Bromide ions are generated once the laser is turned on, and QD growth starts. The precursor cations that already exist in the L/L interface area will nucleate with the bromide ions and grow into QD seeds or nanoclusters until the domestic precursors are consumed. This process is illustrated in Figure 2g as the initial stage of QD growth (Stage 0). The spectrometer cannot detect the nuclei or very small seeds due to their limited quantity and PL quantum yield (QY).[43-45] The PL spectra shown around time zero represents the size of the QD seed formed at stage 0. After the initial stage, the PL peak position continuously shifts to longer wavelengths, representing the QD growth. This can be observed in the contour plot in Figure 2a, where the PL peak shifts to higher wavelengths, accompanied by an increase in PL intensity. Additional nucleation is likely prevented by the separation of cations and anions. The increasing PL intensity is hence attributed to the higher PLQY of larger QDs, since they are more defect-tolerant.[46,47]

To provide further insights into the reaction kinetics, we extracted the peak positions and full-width half maximum (FWHM) as a function of reaction time (Figure 2b). Details of the time interval for spectra collection can be found in the Methods Section in the Supporting Information. The growth of $CsPbBr_3$ perovskite QDs in the first ~ 5 minutes after the rapid formation of QD seeds is much slower than unrestricted QD growth, which typically takes only sub-seconds.[49] This suggests a regulated growth on the L/L interface resulting from the constrained diffusion of precursors. This process is illustrated in Figure 2g as Stage 1. At this stage, the precursor ions in the L/L interface area were already consumed, and further growth relies on the restricted diffusion of precursor ions from outside the L/L interface. The decreasing FWHM of PL from QDs also indicates that the QD growth is size-focused, consistent with the diffusion-controlled colloidal QD growth.[48] According to the reported size curve,[24] in Stage 1 (for M1), the average size of QDs has increased by only ~ 1.1 nm (estimated by the empirical sizing curve of $CsPbBr_3$ QDs). This is comparable to the growth rate of conventional II-VI or III-V QDs.[49-51] A similar growth kinetic trend was obtained from a separate M1 reaction performed at a high temporal resolution (spectra were recorded at 600 ms intervals), as shown in Figure 2c. The higher temporal resolution provides more insight into how the PL peak position red-shifts gradually in the early regime of stage 1 (10^{-2} to 10^{-1} min), attributed to the regulated diffusion of the precursor ions, specifically Pb^{2+} and Cs^{+}, which is further discussed in the ensuing section.

The unique configuration of the micropipette promises asymmetric diffusion processes for separated ionic precursors: cation diffusions are more restricted in the narrow micropipette tip, whereas anion diffusions in the organic phase are less constrained. To verify the ion diffusion processes, we performed a finite volume simulation. Figure 2e shows the simulated mass fraction gradients of precursor ions, assuming cations and stoichiometrically equivalent anions were entirely consumed at the L/L interface area (note that bromide anions are constantly generated in the vicinity of L/L interface from photolysis, more details and parameters are provided in the Supporting Information, Methods and Figure S6). The Br^- diffusion field is hemispherical, whereas the cationic precursor ions diffuse linearly towards the tip aperture as obtained from the simulation. The Br^- mass fraction change across the non-polar reservoir remains almost consistent at 0° and at 45° with the pipette tip, indicating a homogeneous Br^- flux towards the L/L interface from all directions in the non-polar reservoir (Figure 2f). The photolysis of bromobenzene near the interface area generates a constant supply of Br^- indicated by the mass fraction plateau (Figure 2f) spanning ~1.5 µm in the reservoir near the pipette tip. In contrast, in the case of Cs^+ and Pb^{2+}, the supply of ions is limited by the diffusion gradient inside the pipette. The cationic mass fractions decrease gradually as the tip is approached (until ~20 µm) before a sharper decline at ~15 µm from the interface. The low cation concentration near the L/L interface, combined with a lengthy diffusion field, implies that the diffusion of cations is more restricted and can determine the QD growth kinetics.

The rate of PL peak evolution slows down after stage 1, while the FWHM continues to decrease. This is expected since the growth of larger QDs requires even more precursors, and the constrained precursor diffusion will no longer support QD growth at the same rate as in Stage 1 (Figure 2b and Figure 2g). In the following ~ 10 minutes (Stage 2), the PL peak of QDs only shifts ~ 4 nm, and the FWHM is reduced from 22 nm to a minimum value of 18 nm (Figure 2b). This is consistent with the feature of a size-focused diffusion-controlled QD growth. Notably, both homogeneous and inhomogeneous broadening contribute to the FWHM of QDs. While size-focusing growth can reduce inhomogeneous broadening, homogeneous broadening can still contribute up to 5 nm of FHWM, decreasing in Stage 1.[52,53] After Stage 2, the PL peak redshifts and broadens over time. This suggests a ripening process (Stage 3, Figure 2b and Figure 2g) in which the larger QDs consume the monomers generated from the degradation of the smaller QDs. Therefore, a confined L/L interface allowed us to slow down the growth kinetics of $CsPbBr_3$ QDs into three discrete stages that closely follow the LaMer model.

Our protocol spatially separates the nucleation and seed growth from the diffusion-controlled growth since the precursors can only meet at the interface area. Such a nanoscale synthesis contrasts with macroscopic synthesis, in which nucleation and complete growth happen asynchronously in the homogeneous reaction conditions. The nano-confined interfacial synthesis allows regulation of the growth kinetics by simply manipulating the diffusion field. This is demonstrated by conducting the synthesis using M2 and M3 with smaller tip openings than M1. It is worth mentioning that the L/L interface migration is suppressed by sealing the open end of the micropipettes. The QD growth kinetics extracted from the reaction using all three pipettes are plotted in Figure 2d. When narrower pipettes are used, the initial PL peak positions significantly blue shift, appearing at around 463 nm and 453 nm for M2 and M3, respectively (Figure 2d), indicating the formation of smaller QD seeds. This is expected since, as the lateral size of the L/L interface decreases from M1 to M3, the initial precursors available for the seeds to grow also decrease. In contrast, performing the reaction in a microcapillary with a tip opening of ~ 1.4 mm (Figure S2) immediately leads to larger (~ 12 nm) $CsPbBr_3$ QD formation. Interestingly, reducing pressures in the pipette led to a larger QD seed. This can be attributed to

the expansion of the L/L interface when it was retracted into the pipette tip shank (Figure S2). The pressure-sensitive nucleation kinetics agree with the tip size-dependent initial PL position in Figure 2d. It is worth mentioning that the 453 nm QD seeds from M3 can be attributed to metastable nanoclusters, which are in good agreement with previous reports[25,56], suggesting the potential control over the nucleation kinetics of perovskite QDs by engineering the dimensions of the micropipette.

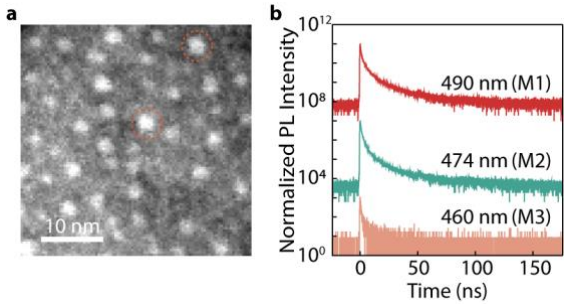

Figure 3. a) Scanning Transmission Electron Microscope (STEM) image of the as-synthesized $CsPbBr_3$ QDs. Two QDs have been marked, which have a size of ~ 2.7 nm and ~ 2.9 nm. b) Time-dependent PL intensity trace of QDs emitting at 490 nm, 474 nm, and 460 nm collected at ~ 1 minute of reaction in M1, M2, and M3 pipettes, respectively.

Apart from the reduced size of QD seeds obtained in Stage 0, the growth kinetics of QDs at Stage 1 were successfully regulated by the tip size of the micropipettes. As shown in Figure 2d, the Stage 1 growth time was extended to around 10 minutes and 12 minutes when M2 and M3 pipettes were used, respectively. This is attributed to the more restricted diffusion of the precursors in the polar phase of narrower pipettes, which agrees with the diffusion-controlled QD growth model discussed above. The derivative of the size evolution curves yields the growth rate, as shown in Figure S4, which clearly demonstrates the regulatory effect of diffusion control in micropipettes. Some practical uncertainties can also affect the growth dynamics. For example, QDs synthesized on the L/L interface may accumulate in the interface area, thus blocking the ion diffusion. However, we have observed that some QDs can be occasionally attached to the inner glass pipette wall, potentially due to the exposure of the polar QD surface without sufficient organic ligand passivation. Nevertheless, the QD growth kinetics are consistent over individual measurements (Figure S5).

The slow growth kinetics allow the isolation of small perovskite QDs at the early stage. QDs can be collected by retracting the pipette from the organic phase and applying pressure on the open end of the pipette or by gently breaking the tip. Figure 3a shows the scanning transmission electron microscope image of QDs obtained within 1 min of the reaction using the M3 pipette. The QDs have an average size of 2.7 nm with a moderate size distribution (19%) (Figure S7). This is attributed to the broader size distributions at the early stage of the reaction, corroborated by the broader FWHM (Figure S4). Elemental analysis using ICP-MS yields a Cs:Pb ratio of 0.83:1, consistent with the reported stoichiometry (QDs synthesized using an M1 pipette, ~ 10 nm in diameter).[42,54] The QDs also do not have a regular shape, which can be partly due to the absence of long-chain ligands, which typically generate cuboidal-shaped QDs in conventional synthetic methods.[55,56] PL lifetime of QDs collected from reactions in all three pipettes three pipettes (Figure 3b) indicates the absence of an organic ligand-passivated QD surface, which is characterized by a multiexponential PL intensity decay with a rapid (~1 ns) component (Supporting Information, Table S1). The absence of ligands leads to directly exposed crystal defects on the QD surface, thereby increasing the non-radiative channels and reducing the excitonic lifetime. Commonly used bulky organic ligands, such as oleylamine and oleic acid, increase the viscosity of the non-polar phase and tend to solidify at the L/L interface, which can hinder kinetic studies. However, organic ligands can passivate surface defects and enhance the colloidal stability of QDs. Therefore, future studies should benefit from the introduction of designer ligands with bipolar ligand tails to enhance the PL efficiency and prevent potential QD aggregations.

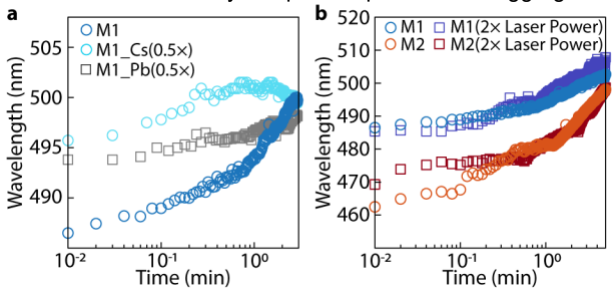

Figure 4. Concentration-dependent growth kinetics of $CsPbBr_3$ QDs on different L/L interfaces: a) PL peak time trace for reactions in stage 1 with Cs and Pb precursor concentrations reduced to half the original value (0.02 M for Pb^{2+} and 0.03 M for Cs^+). b) The PL peak time trace extracted from reactions with the laser power density doubled compared to the original value (60 W/cm^2).

To further investigate the effect of regulated and asymmetric diffusion fields on the reaction kinetics, precursor concentration-dependent QD growth kinetics were measured by fixing the tip size (M1) and changing the precursor concentrations. Firstly, reactions were performed with half of the original concentrations of Cs^+ or Pb^{2+} (details in Supporting Information, Methods), and their corresponding QD growth kinetics in the diffusion-limited stage 1 are plotted in Figure 4a. Both reactions are significantly slowed down, indicated by the smaller shift in PL peak over time (~ 5 nm over 3 min, compared to ~ 15 nm for the reaction with the original Cs^+ and Pb^{2+} concentrations). This is because the diffusion of Pb^{2+} and Cs^+ becomes further limited upon reducing their concentrations. The slightly larger QD seeds generated at the beginning of stage 1 for the Cs^+ or Pb^{2+} deficient reactions can be attributed to fewer nucleation events in stage 0. The effect of Br^- concentration change on the reaction rates was also explored by tuning the laser power. In contrast, the QD growth kinetics in Stage 1 exhibited no significant change even when the laser power was two times higher than the original conditions (Figure 4b). Note that increasing the laser power may have introduced a heating effect that disturbs the soft L/L interface, thereby affecting the initial nucleation and introducing considerable uncertainty during peak position identification. In addition, the larger discrepancy of PL positions from the low signal-to-noise ratio in measurements using M2 micropipette is partially a result of the low PLQY of very small QDs or QD seeds compared to larger QDs, which tend to have higher PLQY. Thus, the larger QDs could contribute more to the PL intensities, leading to an apparent red shift of the PL peak. Nevertheless, the QD growth kinetics in

Stage 1 are almost identical between the two laser power conditions, and such Br^- concentration independence is preserved when different sizes of micropipettes are used. This is consistent with the asymmetric diffusion fields. It is also worth noting that syntheses attempted using low laser power densities (30 W/cm² and 15 W/cm²) did not yield sufficient QDs that can be monitored using PL spectra due to the limited detection efficiency of the optical microscope. However, it is possible that when the laser power is sufficiently low, the bromide generation rate may no longer support the nucleation or QD growth. Additionally, we note that the assumptions made for bromobenzene photolysis kinetics are that it is proportional to the laser power, and other catalytic processes are not considered for the sake of modelling simplicity. These assumptions may no longer be suitable when the laser power is very low. Future studies may utilize theta-pipettes with dual microchannels to control ion diffusion and study the QD growth more independence.

In summary, we bring forth a novel synthetic approach to physically regulate the growth kinetics of $CsPbBr_3$ QDs using a nano-sized L/L interface. The constrained diffusion field inside the micropipettes allows the study of the reaction kinetics using in-situ PL measurements, revealing three discrete stages closely following the LaMer model. Moreover, the QD growth rate and size can be effortlessly controlled by tuning the micropipette tip sizes. The physically separated perovskite nanocrystal nucleation and diffusion-controlled growth successfully retarded perovskite QD growth and provided insights into their growth mechanism without the interferences of coordinating chemicals and ionic precursors. Our study also promises the precise controlled micro-synthesis of perovskite QDs for printing photonics and quantum light sources on chips on demand.

Experimental Section

Materials

Borosilicate capillaries were procured from Drummond (100 µL micropipettes). Lead acetate trihydrate ($Pb(CH_3COO)_2{\cdot}3H2O$, >99.99%), bromobenzene (C_6H_5Br, >99.5%) and anhydrous *N,N*-dimethylformamide (>99.8%) were purchased from Sigma Aldrich. Cesium acetate ($Cs(CH_3COO)$, >99.998%) was purchased from Thermo-Scientific. All chemicals were used without further purification.

Synthetic protocols

Fabrication of the micropipettes: The micropipettes were fabricated using a Sutter P-2000 micropipette puller (Sutter Instrument, Novato, CA, USA) using the following pulling programs:

Pipette	Heat	Filament	Velocity	Delay	Pull
M1	325	0	20	250	80
M2	325	0	25	250	80
M3	325	0	25	250	90

Preparation of the polar precursor solution: 25 mg of lead acetate trihydrate and 25 mg of cesium acetate were dissolved in 4 mL of dimethylformamide (DMF) and vortexed until all the solids dissolved to form a clear solution containing 20 mM of Pb^{2+} and 30 mM of Cs^+.

Preparation of the nonpolar phase: The nonpolar phase was composed of neat bromobenzene. Br^- are generated through photolysis when this phase is exposed to the 405 nm laser.

Synthesis of $CsPbBr_3$ QDs at the L/L interfaces supported in micropipettes: 30 µL of the polar phase is loaded into the micropipette from the broad end using a microliter syringe. The air bubbles that may have been trapped at the tip were removed by gently shaking the pipette and then the broad end is sealed using wax. The micropipette tip is then immersed into the non-polar phase (1 mL of bromobenzene), to establish the L/L interface. The 405 nm laser is focused on the tip area using an objective lens (LEICA 518129 with a 40x magnification and numerical aperture of 0.5) to initiate the reaction. The $CsPbBr_3$ QDs then start generating at the tip area, and the corresponding photoluminescence (PL) emission is collected using the same objective lens and guided to a modular spectrometer.

Transmission Electron Microscope (TEM) sample preparation: The QDs in the pipette tips were deposited onto carbon-coated copper TEM grids by gently breaking the tip on the surface of the grid. Multiple pipettes with the same tip diameter were used for each grid.

Concentration-dependent studies: For 0.5x Lead acetate solution, 12.5 mg of lead acetate trihydrate and 25 mg of cesium acetate were dissolved in 4 ml of dimethylformamide (DMF) and vortexed until all the solids dissolved to form a solution containing 10 mM of Pb^{2+} and 30 mM of Cs^+.

For 0.5x Cs^+ solution, 25 mg of lead acetate trihydrate and 12.5 mg of cesium acetate were dissolved in 4 ml of dimethylformamide (DMF) and vortexed until all the solids dissolved to form a solution containing 20 mM of Pb^{2+} and 15 mM of Cs^+.

The laser power density was increased to 120 W/cm^2 for bromide concentration-dependent studies and set to 60 W/cm^2 for all other measurements.

Pressure-dependent studies: 30 µL of the polar phase is loaded into the micropipette from the broad end using a microliter syringe. The air bubbles that may have been trapped at the tip were removed by gently shaking the pipette and then the broad end is left open. The micropipette tip is then immersed into the non-polar phase (1 mL of bromobenzene), to establish the L/L interface. A positive or a negative pressure is applied using a syringe pump through the open end of the pipette. The 405 nm laser is focused on the tip area using an objective lens (LEICA 518129 with a 40x magnification and numerical aperture of 0.5) to initiate the reaction. The $CsPbBr_3$ QDs then start generating at the tip area, and the corresponding photoluminescence (PL) emission is collected using the same objective lens and guided to a modular spectrometer.

ICP-MS studies: The QDs generated at the micropipette tip are dissolved in concentrated nitric acid (67%) by dipping the pipette tip in it. The QD-nitric acid solution is diluted to around 350 times and then analyzed using ICP-MS.

Finite volume modelling

A steady-state two-dimensional axisymmetric computational model was developed for prediction of the ion diffusion in the micropipette. The diffusion of species *i* in an isothermal

multicomponent mixture with constant density and diffusion coefficients is described by the following equation:

$$\rho D_{m,i}\left[\frac{1}{r}\frac{\partial}{\partial r}\left(r\frac{\partial Y_i}{\partial r}\right)+\frac{\partial}{\partial z}\left(\frac{\partial Y_i}{\partial z}\right)\right]+S_i=0$$

where ρ is the mixture density, $D_{m,i}$ and Y_i are the mass diffusion coefficient of species *i* in the mixture, and mass fraction of species *i*, and S_i is the source term accounting for consumption or generation of species *i* due to reaction. For a dilute multicomponent mixture like the mixture in the pipette, $D_{m,i}$ is the binary diffusion coefficient of the species *i* in the solvent (DMF).

The computational domain is shown in Figure S6. Due to symmetry, the pipette is modeled as a two-dimensional domain revolving around the horizontal axis. The tip of the pipette where it touches the reservoir has a diameter of 1.6 µm. The diameter of the pipette far from the entrance is 10 µm. The length of the pipette considered in the simulation is 40 µm. The hemispherical reservoir has a diameter of 20 µm. A hemispherical zone near the pipette tip in the reservoir with a diameter of about 4 µm ("illuminated zone" in Fig. S6) is illuminated by 405 nm laser to create bromide ions from bromobenzene. The rest of the reservoir is illuminated with an intensity of about one-sixth of the illuminated zone.

Due to the small size of the system, solving the governing equation using the actual dimensions will lead to significant roundoff errors and will deteriorate the numerical accuracy of the results. To overcome this issue, the equation can be nondimensionalized by introducing the following non-dimensional variables:

$$r^*=\frac{r}{R}\qquad z^*=\frac{z}{R}\qquad S^*=S\left(\frac{R^2}{\rho D}\right)$$

where *R*, ρ, and *D,* are characteristic length, density and diffusion coefficient, respectively. It is noted that the dependent variable, mass fraction *Y*, is already dimensionless and as such the mass fractions obtained from the non-dimensional solution are the same as those obtained from the solution of the dimensional version of the equation. Substituting the dimensional variables using their non-dimensional counterparts, the governing equation in non-dimensional format can be obtained:

$$\frac{1}{r^*}\frac{\partial}{\partial r^*}\left(r^*\frac{\partial Y_i}{\partial r^*}\right)+\frac{\partial}{\partial z^*}\left(\frac{\partial Y_i}{\partial z^*}\right)+S_i^*=0$$

Boundary conditions:

The boundary conditions are obtained from the experimental study. They include the consumption rate of the ions, namely Pb^{2+} and Cs^+ in the pipette and Br^- in the reservoir, at the liquid-liquid (L/L) interface, plus the mass fractions of the Br^- in the reservoir far from the L/L interface, and mass fractions of the Pb^{2+} and Cs^+ at the L/L interface. In the pipette, both the consumption rate and mass fractions of Pb^{2+} and Cs^+ are approximated at the L/L interface. However, since there is no source term for these ions along the pipette, the same mass transfer rates prevail along the entire pipette length. The boundary conditions are as follows:

Far end of the pipette:

Pb^{2+}: mass flux = consumption rate of Pb^{2+}/surface area of the far end of the pipette

Cs^+: mass flux = consumption rate of Cs^+/surface area of the far end of the pipette

Br^-: mass fraction = 0

L/L interface:

Pb^{2+}: mass fraction = 0

Cs^+: mass fraction = 0

Br^-: mass flux = consumption rate of Br^-/surface area of the L/L

Far boundary of the reservoir:

Pb^{2+}: mass fraction = 0

Cs^+: mass fraction = 0

Br^-: mass fraction = 0

The experimentally determined consumption rates of the ions at the L/L were 4.9×10^{-20} kg/s, 3.1×10^{-20} kg/s, and 5.7×10^{-20} kg/s for Pb^{2+}, Cs^+, and Br^-, respectively. The corresponding mass fluxes were calculated by dividing the consumption rates by the respective surface areas. The non-dimensional mass fluxes are calculated by multiplying the dimensional ones by $R/(\rho D_{m,i})$ where ρ and $D_{m,I}$ are the related density and mass diffusion coefficients. The employed non-dimensional mass flux boundary conditions are listed in the following:

Far end of the pipette:

Pb^{2+}: non-dimensional mass flux, $\partial Y_{Pb^{2+}}/\partial z^* = -2.9\times10^{-9}$

Cs^+: non-dimensional mass flux, $\partial Y_{Cs^+}/\partial z^* = -2.6\times10^{-9}$

L/L interface:

Br^-: non-dimensional mass flux, $\partial Y_{Br^-}/\partial z^* = 1.8\times10^{-7}$

The dimensionless source terms for Br^- in the illuminated zone and the rest of the reservoir were 5.2×10^{-5} and 8.6×10^{-6}, respectively, corresponding to 0.8 and 0.13 kg/(m^3·s).

The dimensionless governing equations and related boundary conditions are solved using a control volume approach implemented in ANSYS Fluent version 2025 R1. diffusion in the reservoir was found to be non-linear.

Characterizations

The in-situ PL measurements were obtained using a custom-built microscope coupled with an Oceanview USB 4000 spectrometer, as illustrated in Figure S1. All measurements were done under ambient conditions and room temperature. A 405 nm laser source (Coherent OBIS LX) was used to excite the QDs.

For the in-situ PL measurements, the integration time was set to 600 ms, and the spectra were recorded at an interval of 600 ms. For longer in-situ measurements spectra were recorded at an interval of 30 s. The same parameters were used for the bromide precursor concentration dependence study. For Cs and Pb precursor concentration-dependent studies, the integration time was set to 1 s, and the spectra were recorded at intervals of 1 s as well.

The PL lifetime was measured with time-correlated single photon counting method on a customized epi-illuminating fluorescence microscope. A 405 nm diode laser was focused by an objective lens (Olympus UPLXAPO100XO, 100× magnification, NA = 1.45) to excite the sample (Picoquant LDH-D-C-405, driven by a Picoquant Sepia PDL828 module). The emission was collected using the same objective, pass through a 405 nm notch filter and a 425 nm long-pass filter, and measured by a single-photon avalanche diode (Hamamatsu C11202-100) connected to a time-correlator (Picoquant HydraHarp 400).

TEM measurements were performed on a Titan Themis 300.

ICP-MS was performed on a Perkin Elmer Nexion 2000

Supporting Information

Supporting figures are provided in the Supporting Information.

Acknowledgements

This material is based upon work supported by the National Science Foundation (NSF), under Award Number 2316919. Use of the TAMU Materials Characterization Facility (RRID: SCR_022202) and Dr. Sisi Xiang are acknowledged. SEM data collection was performed by Dr. Preston Larson at the Samuel Roberts Noble Microscopy Laboratory, a University of Oklahoma (OU) core facility supported by the Vice President for Research and Partnerships. We also thank Dr. Hyunho Noh for providing discussions.

Conflict of interest

The authors declare no competing financial interests.

Data Availability

The data that support the findings of this study are available from the corresponding author upon reasonable request.

Keywords: Growth kinetics • Liquid/Liquid interface • Micro-synthesis • Micropipette • Perovskite quantum dots

References

[1] Kovalenko, M. V., Protesescu, L. & Bodnarchuk, M. I. Properties and potential optoelectronic applications of lead halide perovskite nanocrystals. *Science* **358**, 745-750 (2017). https://doi.org/doi:10.1126/science.aam7093

[2] Dey, A. *et al.* State of the Art and Prospects for Halide Perovskite Nanocrystals. *ACS Nano* **15**, 10775-10981 (2021). https://doi.org/10.1021/acsnano.0c08903

[3] Shamsi, J., Urban, A. S., Imran, M., De Trizio, L. & Manna, L. Metal Halide Perovskite Nanocrystals: Synthesis, Post-Synthesis Modifications, and Their Optical Properties. *Chemical Reviews* **119**, 3296-3348 (2019). https://doi.org/10.1021/acs.chemrev.8b00644

[4] Dong, Y. *et al.* Bipolar-shell resurfacing for blue LEDs based on strongly confined perovskite quantum dots. *Nature Nanotechnology* **15**, 668-674 (2020). https://doi.org/10.1038/s41565-020-0714-5

[5] Fakharuddin, A. *et al.* Perovskite light-emitting diodes. *Nature Electronics.* **5**, 203-216 (2022). https://doi.org/10.1038/s41928-022-00745-7

[6] Han, T.-H. *et al.* A roadmap for the commercialization of perovskite light emitters. *Nature Reviews Materials.* **7**, 757-777 (2022). https://doi.org/10.1038/s41578-022-00459-4

[7] Rainò, G. *et al.* Superfluorescence from lead halide perovskite quantum dot superlattices. *Nature* **563**, 671-675 (2018). https://doi.org/10.1038/s41586-018-0683-0

[8] Cherniukh, I. *et al.* Perovskite-type superlattices from lead halide perovskite nanocubes. *Nature* **593**, 535-542 (2021). https://doi.org/10.1038/s41586-021-03492-5

[9] Sekh, T. V. *et al.* All-Perovskite Multicomponent Nanocrystal Superlattices. *ACS Nano* **18**, 8423-8436 (2024). https://doi.org/10.1021/acsnano.3c13062

[10] Kang, J. & Wang, L.-W. High Defect Tolerance in Lead Halide Perovskite $CsPbBr_3$. *The Journal of Physical Chemistry Letters* **8**, 489-493 (2017). https://doi.org/10.1021/acs.jpclett.6b02800

[11] Lignos, I. *et al.* Synthesis of Cesium Lead Halide Perovskite Nanocrystals in a Droplet-Based Microfluidic Platform: Fast Parametric Space Mapping. *Nano Letters* **16**, 1869-1877 (2016). https://doi.org/10.1021/acs.nanolett.5b04981

[12] Lv, H., Zheng, Y., Geng, Y., Xu, S. & Geng, C. Insight into the growth kinetics of CsPbBr3 perovskite nanocrystals using an oil-water droplet fluidic synthesis route. *Chemical Engineering Journal* **480**, 148315 (2024). https://doi.org/https://doi.org/10.1016/j.cej.2023.148315

[13] Koolyk, M., Amgar, D., Aharon, S. & Etgar, L. Kinetics of cesium lead halide perovskite nanoparticle growth; focusing and de-focusing of size distribution. *Nanoscale* **8**, 6403-6409 (2016). https://doi.org/10.1039/C5NR09127F

[14] Chakrabarty, A., Satija, S., Gangwar, U. & Sapra, S. Precursor-Mediated Synthesis of Shape-Controlled Colloidal $CsPbBr_3$ Perovskite Nanocrystals and Their Nanofiber-Directed Self-Assembly. *Chemistry of Materials* **32**, 721-733 (2020). https://doi.org/10.1021/acs.chemmater.9b03700

[15] Li, Y., Huang, H., Xiong, Y., Kershaw, S. V. & Rogach, A. L. Revealing the Formation Mechanism of $CsPbBr_3$ Perovskite Nanocrystals Produced via a Slowed-Down Microwave-Assisted Synthesis. *Angewandte Chemie International Edition* **57**, 5833-5837 (2018). https://doi.org/https://doi.org/10.1002/anie.201713332

[16] Wen, J.-R. *et al.* Chemical Availability of Bromide Dictates $CsPbBr_3$ Nanocrystal Growth. *Chem. Mater.* **31**, 8551-8557 (2019). https://doi.org/10.1021/acs.chemmater.9b03709

[17] Akkerman, Q. A. *et al.* Solution Synthesis Approach to Colloidal Cesium Lead Halide Perovskite Nanoplatelets with Monolayer-Level Thickness Control. *Journal of the American Chemical Society* **138**, 1010-1016 (2016). https://doi.org/10.1021/jacs.5b12124

[18] Dong, Y. *et al.* Controlling Anisotropy of Quantum-Confined $CsPbBr_3$ Nanocrystals by Combined Use of Equilibrium and Kinetic Anisotropy. *Chemistry of Materials* **31**, 5655-5662 (2019). https://doi.org/10.1021/acs.chemmater.9b01515

[19] Pradhan, N. Growth of Lead Halide Perovskite Nanocrystals: Still in Mystery. *ACS Physical Chemistry Au* **2**, 268-276 (2022). https://doi.org/10.1021/acsphyschemau.2c00001

[20] LaMer, V. K. & Dinegar, R. H. Theory, Production and Mechanism of Formation of Monodispersed Hydrosols. *Journal of the American Chemical Society* **72**, 4847-4854 (1950). https://doi.org/10.1021/ja01167a001

[21] Thanh, N. T. K., Maclean, N. & Mahiddine, S. Mechanisms of Nucleation and Growth of Nanoparticles in Solution. *Chemical Reviews* **114**, 7610-7630 (2014). https://doi.org/10.1021/cr400544s

[22] Murray, C. B., Kagan, C. R. & Bawendi, M. G. Synthesis and Characterization of Monodisperse Nanocrystals and Close-Packed Nanocrystal Assemblies. *Annual Review of Materials Research* **30**, 545-610 (2000). https://doi.org/https://doi.org/10.1146/annurev.matsci.30.1.545

[23] Li, F. *et al.* Controlled Growth of $CH_3NH_3PbBr_3$ Perovskite Nanocrystals via a Water–Oil Interfacial Synthesis Method. *Angewandte Chemie International Edition* **58**, 17631-17635 (2019). https://doi.org/https://doi.org/10.1002/anie.201910225

[24] Akkerman, Q. A. *et al.* Controlling the nucleation and growth kinetics of lead halide perovskite quantum dots. *Science* **377**, 1406-1412 (2022). https://doi.org/doi:10.1126/science.abq3616

[25] Atteberry, M. L., Mi, C., Chandra, S., Hidayatova, L. & Dong, Y. Unraveling the Growth Mechanism of Strongly Confined $CsPbBr_3$ Perovskite Quantum Dots under Thermodynamic Equilibrium Control. *Chemistry of Materials* **36**, 4521-4529 (2024). https://doi.org/10.1021/acs.chemmater.4c00160

[26] Montanarella, F. *et al.* Growth and Self-Assembly of $CsPbBr_3$ Nanocrystals in the TOPO/$PbBr_2$ Synthesis as Seen with X-ray Scattering. *Nano Letters* **23**, 667-676 (2023). https://doi.org/10.1021/acs.nanolett.2c04532

[27] Sun, C., Jiang, Y., Zhang, L., Wei, K. & Yuan, M. Toward the Controlled Synthesis of Lead Halide Perovskite Nanocrystals. *ACS Nano* **17**, 17600-17609 (2023). https://doi.org/10.1021/acsnano.3c05609

[28] Brown, A. A. M. *et al.* Precise Control of $CsPbBr_3$ Perovskite Nanocrystal Growth at Room Temperature: Size Tunability and Synthetic Insights. *Chemistry of Materials* **33**, 2387-2397 (2021). https://doi.org/10.1021/acs.chemmater.0c04569

[29] Protesescu, L. *et al.* Nanocrystals of Cesium Lead Halide Perovskites ($CsPbX_3$, X = Cl, Br, and I): Novel Optoelectronic Materials Showing Bright Emission with Wide Color Gamut. *Nano Letters* **15**, 3692-3696 (2015). https://doi.org/10.1021/nl5048779

[30] Dong, Y. *et al.* Precise Control of Quantum Confinement in Cesium Lead Halide Perovskite Quantum Dots via Thermodynamic Equilibrium. *Nano Letters* **18**, 3716-3722 (2018). https://doi.org/10.1021/acs.nanolett.8b00861

[31] Fiuza-Maneiro, N. *et al.* Ligand Chemistry of Inorganic Lead Halide Perovskite Nanocrystals. *ACS Energy Letters* **8**, 1152-1191 (2023). https://doi.org/10.1021/acsenergylett.2c02363

[32] Morad, V. *et al.* Designer phospholipid capping ligands for soft metal halide nanocrystals. *Nature* **626**, 542-548 (2024). https://doi.org/10.1038/s41586-023-06932-6

[33] Mi, C. *et al.* Towards non-blinking and photostable perovskite quantum dots. *Nature Communications* **16**, 204 (2025). https://doi.org/10.1038/s41467-024-55619-7

[34] Sun, S., Yuan, D., Xu, Y., Wang, A. & Deng, Z. Ligand-Mediated Synthesis of Shape-Controlled Cesium Lead Halide Perovskite Nanocrystals via Reprecipitation Process at Room Temperature. *ACS Nano* **10**, 3648-3657 (2016). https://doi.org/10.1021/acsnano.5b08193

[35] De Roo, J. *et al.* Highly Dynamic Ligand Binding and Light Absorption Coefficient of Cesium Lead Bromide Perovskite Nanocrystals. *ACS Nano* **10**, 2071-2081 (2016). https://doi.org/https://doi.org/10.1021/acsnano.5b06295

[36] Perry, D., Parker, A. S., Page, A. & Unwin, P. R. Electrochemical Control of Calcium Carbonate Crystallization and Dissolution in Nanopipettes. *ChemElectroChem* **3**, 2212-2220 (2016). https://doi.org/https://doi.org/10.1002/celc.201600547

[37] Mondaca-Medina, E. *et al.* Nanoelectrochemistry in electrochemical phase transition reactions. *Chemical Science* **14**, 7611-7619 (2023). https://doi.org/10.1039/D3SC01857A

[38] Li, Y. *et al.* Method To Directly Measure and Actively Control a Single Nucleation-Crystal Growth Process. *Crystal Growth & Design* **19**, 2470-2475 (2019). https://doi.org/10.1021/acs.cgd.9b00151

[39] Liu, S., Li, Q. & Shao, Y. Electrochemistry at micro- and nanoscopic liquid/liquid interfaces. *Chemical Society Reviews* **40**, 2236-2253 (2011). https://doi.org/10.1039/C0CS00168F

[40] Košmrlj, B. & Šket, B. Photolysis of Bromo- and Chloro-Substituted Benzyl Derivatives. Competition between Ionic and Radical Pathways. The *Journal of Organic Chemistry* **65**, 6890-6896 (2000). https://doi.org/10.1021/jo0001481

[41] Behera, B. & Das, P. HCl elimination in the photolysis of chlorobenzene at 266 nm: An FT-IR spectroscopy and quantum chemical study. *Chemical Physics Letters* **774**, 138601 (2021). https://doi.org/https://doi.org/10.1016/j.cplett.2021.138601

[42] Maes, J. *et al.* Light Absorption Coefficient of $CsPbBr_3$ Perovskite Nanocrystals. *The Journal of Physical Chemistry Letters* **9**, 3093-3097 (2018). https://doi.org/10.1021/acs.jpclett.8b01065

[43] Guarino-Hotz, M. *et al.* Structural Study of Paraffin-Stabilized Methylammonium Lead Bromide Magic-Sized Clusters. *The Journal of Physical Chemistry C* **127**, 3367-3376 (2023). https://doi.org/10.1021/acs.jpcc.2c08645

[44] Vickers, E. T. *et al.* Ligand Dependent Growth and Optical Properties of Hybrid Organo-metal Halide Perovskite Magic Sized Clusters. *The Journal of Physical Chemistry C* **123**, 18746-18752 (2019). https://doi.org/10.1021/acs.jpcc.9b05521

[45] Udayabhaskararao, T., Kazes, M., Houben, L., Lin, H. & Oron, D. Nucleation, Growth, and Structural Transformations of Perovskite Nanocrystals. *Chemistry of Materials* **29**, 1302-1308 (2017). https://doi.org/10.1021/acs.chemmater.6b04841

[46] Ye, J. *et al.* Strongly-confined colloidal lead-halide perovskite quantum dots: from synthesis to applications. *Chemical Society Reviews* **53**, 8095-8122 (2024). https://doi.org/10.1039/D4CS00077C

[47] Huang, H., Bodnarchuk, M. I., Kershaw, S. V., Kovalenko, M. V. & Rogach, A. L. Lead Halide Perovskite Nanocrystals in the Research Spotlight: Stability and Defect Tolerance. *ACS Energy Letters* **2**, 2071-2083 (2017). https://doi.org/10.1021/acsenergylett.7b00547

[48] Yin, Y. & Alivisatos, A. P. Colloidal nanocrystal synthesis and the organic–inorganic interface. *Nature* **437**, 664-670 (2005). https://doi.org/10.1038/nature04165

[49] Dagtepe, P., Chikan, V., Jasinski, J. & Leppert, V. J. Quantized Growth of CdTe Quantum Dots; Observation of Magic-Sized CdTe Quantum Dots. The *Journal of Physical Chemistry C.* **111**, 14977-14983 (2007). https://doi.org/10.1021/jp072516b

[50] Xue, X., Huang, Y., Zhuang, Z., Huang, F. & Lin, Z. Temperature-sensitive growth kinetics and photoluminescence properties of CdS quantum dots. *CrystEngComm.* **15**, 4963-4969 (2013). https://doi.org/10.1039/C3CE40478A

[51] Lazzari, S., Abolhasani, M. & Jensen, K. F. Modeling of the formation kinetics and size distribution evolution of II–VI quantum dots. *Reaction Chemistry and Engineering.* **2**, 567-576 (2017). https://doi.org/10.1039/C7RE00068E

[52] Brennan, M. C. *et al.* Origin of the Size-Dependent Stokes Shift in $CsPbBr_3$ Perovskite Nanocrystals. *J. Am. Chem. Soc.* **139**, 12201-12208 (2017). https://doi.org/10.1021/jacs.7b05683

[53] Cheng, O. H.-C., Qiao, T., Sheldon, M. & Son, D. H. Size- and temperature-dependent photoluminescence spectra of strongly confined $CsPbBr_3$ quantum dots. *Nanoscale* **12**, 13113-13118 (2020). https://doi.org/10.1039/D0NR02711A

[54] Bodnarchuk, M. I. *et al.* Rationalizing and Controlling the Surface Structure and Electronic Passivation of Cesium Lead Halide Nanocrystals. *ACS Energy Letters* **4**, 63-74 (2019). https://doi.org/10.1021/acsenergylett.8b01669

[55] Liang, Z. *et al.* Shape-Controlled Synthesis of All-Inorganic $CsPbBr_3$ Perovskite Nanocrystals with Bright Blue Emission. *ACS Applied Materials & Interfaces* **8**, 28824-28830 (2016). https://doi.org/10.1021/acsami.6b08528

[56] Kazes, M., Udayabhaskararao, T., Dey, S. & Oron, D. Effect of Surface Ligands in Perovskite Nanocrystals: Extending in and Reaching out. *Accounts of Chemical Research* **54**, 1409-1418 (2021). https://doi.org/10.1021/acs.accounts.0c00712

Entry for the Table of Contents

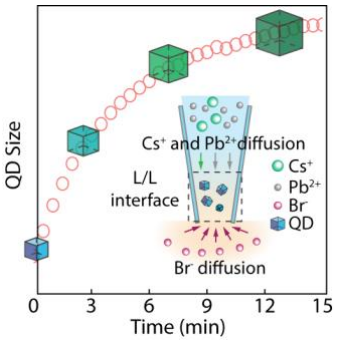

Monitoring the growth kinetics of $CsPbBr_3$ QDs by physically separating the nucleation and growth events. A confined liquid/liquid (L/L) interface was used to achieve slow growth kinetics and the same was monitored through in-situ photoluminescence (PL) spectroscopy. The growth model obtained closely mimics the well-established LaMer model and allows the isolation of very small QDs (2.7 nm).